

The influence of volume constraint method on achieving the exact boundary representation in FEM-based topology optimization: Case studies

Yi CUI¹⁾, Toru TAKAHASHI²⁾, Koichi TAJI³⁾, Toshiro MATSUMOTO⁴⁾

- 1) Nagoya University (〒 464-8603 Furo-cho, Chikusa-ku, Nagoya, E-mail: yi.cui@mae.nagoya-u.ac.jp)
 2) Nagoya University (〒 464-8603 Furo-cho, Chikusa-ku, Nagoya, E-mail: toru.takahashi@mae.nagoya-u.ac.jp)
 3) Nagoya University (〒 464-8603 Furo-cho, Chikusa-ku, Nagoya, E-mail: kouichi.taji@mae.nagoya-u.ac.jp)
 4) Nagoya University (〒 464-8603 Furo-cho, Chikusa-ku, Nagoya, E-mail: t.matsumoto@nuem.nagoya-u.ac.jp)

Intuitively, exact boundary representation would be the most preferable for the finite element method (FEM) based topology optimization of structures. With exact boundary representation, the material domain can be defined in an exact fashion, which allows imposing arbitrary boundary condition on newly generated boundaries during optimization. However, with the conventional method to constrain volume (the Augmented Lagrangian for volume-constrained problems), topology optimization with exact boundary representation encounters convergence issue. This work indicates that the difference between the FEM mesh for the stress equilibrium and that for the reaction-diffusion equation (RDE) of level set function could be responsible for the convergence issue. In addition, the influence of conventional volume constraint on this convergence has been examined in this study.

Key Words: Exact boundary representation, Volume constraint, Topology optimization, Topological derivative, Finite element method

1. Introduction

In the modern manufacturing process, structural topology optimization has been playing a crucial role with the development of computer technology. As a well-established topology optimization approach, the SIMP (solid isotropic material with penalization) method^(1, 2) interpolates material constants by using the distribution of density. In the numerical implementation, a nonzero lower bound of Young's modulus is set to prevent singularity in solving the stress equilibrium equation. To prevent drawbacks of severe degree of grayscale problem in the original SIMP method, the level set method, in particular, the one via solving the reaction diffusion equation (RDE), has been proposed by Yamada et al.⁽³⁾ It has since been viewed as an attracting alternative for various topology optimization problems.^(4, 5, 6, 7, 8, 9) In particular, topology optimizations^(6, 7, 8) using updated body-fitted mesh have been successfully carried out by adopting variations of augmented Lagrangian method for volume-constrained problems. However, in

forementioned studies, mesh inside the void domain is still necessary and a nonzero lower bound is needed to prevent the singularity problem in solving the stress equilibrium equation. As we have showed and compared in the appendix of the recent work⁽⁹⁾, such an approach can achieve convergence even with the conventional volume constraint method since the nonzero lower bound assigned inside void domain (similar to the SIMP method) can help stabilize the optimization process. Unlike in the mainstream body-fitted remeshing approach, exact boundary representation (no mesh assigned in void domain) has barely been achieved. Not to mention that the now widely adopted topological derivative⁽¹⁰⁾ for sensitivity analysis should be associated with the exact boundary representation since it bases on the idea of insertion of holes rather than the distribution of density. The obstacle to achieving exact boundary representation likely arises from adopting the conventional volume constraint method.^(11, 12, 13) In contrast, the recently proposed exact method for volume constraint⁽⁹⁾ has rather enabled such convergence under the exact boundary representation. However, in the

previous work ⁽⁹⁾, whether or not exact boundary representation is achievable by adopting the conventional volume constrain method with different penalty parameters has not been investigated. In addition, the validity of the proposed exact boundary representation has not been examined for an extremely small constraint of volume such as 5% of the design domain, when a deteriorated connectivity of the reconstructed domain Ω could occur due to the sudden drop of the actual material volume. Also, case studies of different aspect ratio of the design domain have not been provided either. Regarding the topology optimization with exact boundary representation, the aim of this work is hence to further investigate the above issues such as the influence of penalty parameters in the conventional volume constraint method, the extreme setup of constrained volume and the aspect ratio of the design domain.

2. The Methodology

To perform the structural topology optimization, first we define the level-set function ϕ . The following level set function ϕ is introduced to represent the material domain Ω , the material boundary $\partial\Omega$ and the complementary void domain $D\setminus\Omega$:

$$\begin{cases} 0 < \phi(\mathbf{x}) \leq 1 & \text{for } \mathbf{x} \in \Omega, \\ \phi(\mathbf{x}) = 0 & \text{for } \mathbf{x} \in \partial\Omega, \\ -1 \leq \phi(\mathbf{x}) < 0 & \text{for } \mathbf{x} \in D\setminus\Omega. \end{cases} \quad (1)$$

A characteristic function as defined below is necessary in performing the volume integration.

$$\chi_\phi = H(\phi) = \begin{cases} 0 & \text{if } \phi < 0, \\ 1 & \text{if } \phi \geq 0. \end{cases} \quad (2)$$

The minimum compliance problem by considering the level set function $\phi(\mathbf{x}) \in [-1, 1]$ as a spatial function inside the design domain can be formulated as follows:

$$\inf_{\phi} F(\phi) = l(\mathbf{u}), \quad (3)$$

$$\text{subject to } a(\mathbf{u}, \mathbf{v}) = l(\mathbf{v}), \quad (4)$$

$$\text{and } G(\phi) = \int_D \chi_\phi \, d\Omega - V_{\text{req}} \leq 0. \quad (5)$$

The weak form of the governing equation reads

$$a(\mathbf{u}, \mathbf{v}) := \int_{\Omega} \boldsymbol{\varepsilon}(\mathbf{u}) : \mathbb{C} : \boldsymbol{\varepsilon}(\mathbf{v}) \, d\Omega, \quad (6)$$

$$l(\mathbf{v}) := \int_{\Gamma_N} \mathbf{t} \cdot \mathbf{v} \, d\Gamma. \quad (7)$$

Here D is the design domain, V_{req} is the volume constraint, \mathbf{u} is the displacement, \mathbf{v} is the virtual displacement, $\boldsymbol{\varepsilon}(\mathbf{u})$ is the corresponding total strain, \mathbb{C} is the fourth-order elasticity tensor and the vector \mathbf{t} is the given external boundary load. Since the boundary representation becomes exact, the same weak form is based on the

reconstructed material domain Ω :

$$\int_{\Omega} \boldsymbol{\varepsilon}(\mathbf{u}) : \mathbb{C} : \boldsymbol{\varepsilon}(\mathbf{v}) \, d\Omega = \int_{\Gamma_N} \mathbf{t} \cdot \mathbf{v} \, d\Gamma. \quad (8)$$

The boundary value problem to update the level set function is as follow.

$$\begin{cases} \frac{\partial \phi}{\partial t} = K(-\bar{\mathcal{T}} + \Lambda + \tau \nabla^2 \phi) & \text{in } D, \\ \frac{\partial \phi}{\partial n} = 0 & \text{on } \partial D \setminus \partial \Gamma_N, \\ \phi = 1 & \text{on } \partial \Gamma_N. \end{cases} \quad (9)$$

Here t is the fictitious time, K is the coefficient of proportionality, τ is a regularization parameter for the fictitious interface energy, and $\bar{\mathcal{T}}$ stands for the topological derivative and can be expressed as:

$$\bar{\mathcal{T}} = -\boldsymbol{\sigma} : \mathbb{P} : \boldsymbol{\varepsilon}. \quad (10)$$

The normalized topological derivative can be expressed as:

$$\begin{cases} \bar{\mathcal{T}} = C_0 \mathcal{T}, \\ C_0 = \frac{\int_D d\Omega}{2 \int_D |\mathcal{T}| d\Omega}. \end{cases} \quad (11)$$

The polarization tensor \mathbb{P} for the plane stress case can be found, for example, in Lopes et al.:⁽¹⁰⁾

$$\mathbb{P} = \frac{1}{1 + \nu} \left(2\mathbb{I} - \frac{1 - 3\nu}{2(1 - \nu)} \mathbf{I} \otimes \mathbf{I} \right). \quad (12)$$

Verification has been made by comparing the above topological derivative with the corresponding result from the direct FEM calculation. During the numerical implementation, it is the normalized topological derivative $\bar{\mathcal{T}}$ that has been used.

Our finite element analysis has been carried out by FreeFEM++,^(14, 15) and it is an open-source software package that requires formulating the weak form of governing equation to carry out the finite element simulation. As for the remeshing process, the open-source software package Mmg has been employed. For illustration, the design domain D , the material domain Ω and the void domain $D\setminus\Omega$ are shown in Fig. 1, alongside the geometry and boundary conditions.

2.1. The augmented Lagrangian method for volume-constrained problems^(11, 12, 13, 16)

The Augmented Lagrangian for volume-constrained problems, as referred as the conventional method, for the current step $t_{n+1} = t + \Delta t$, is formulated as:

$$\Lambda_{n+1} = \begin{cases} \frac{1}{V} (q_n + r_n G_n) & \text{if } G_n \geq -\frac{q_n}{r_n} \\ 0 & \text{if } G_n < -\frac{q_n}{r_n} \end{cases} \quad (13)$$

It should be noted that all above parameters are from the previous optimization step t_n :

$$G_n = \int_D \chi(\phi_n) \, d\Omega - V_{\text{req}}. \quad (14)$$

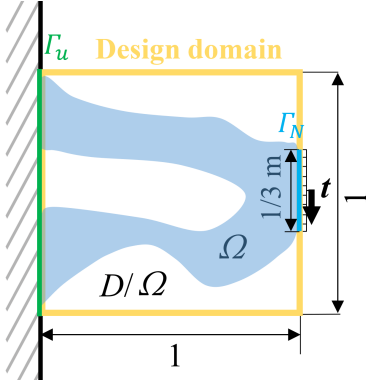


Fig. 1: The schematic illustration of design domain, material domain, complementary void domain and boundary conditions. The aspect ratios for the last two numerical cases are set as 3:1 and 6:1.

Only after knowing the current Λ_{n+1} (and hence ϕ_{n+1}) can all other parameters be updated as follows to be used in the next optimization step. Given the initial values of the two parameters and the constant γ are $q_1 = 0$, $r_1 = 0.1$ or 0.2 and $\gamma = 1.025$., they are updated in the optimization process by:

$$\begin{cases} q_{n+1} = q_n + r_n \max(G_n, -q_n/r_n), \\ r_{n+1} = \gamma r_n. \end{cases} \quad (15)$$

2.2. The exact volume constraint method⁽⁹⁾

The pivotal idea of the exact volume constraint method is to split the original RDE into two terms by letting:

$$\phi = \phi^* + \Lambda \hat{\phi}. \quad (16)$$

Once split, ϕ^* within the interval from t to $t + \Delta t$ is governed by:

$$\begin{cases} \frac{\partial \phi^*}{\partial t} = K(-\bar{T} + \tau \nabla^2 \phi^*) & \text{in } D, \\ \frac{\partial \phi^*}{\partial n} = 0 & \text{on } \partial D \setminus \partial \Gamma_N, \\ \phi^* = 1 & \text{on } \partial \Gamma_N, \\ \phi^*|_t = \phi|_t. \end{cases} \quad (17)$$

By subtracting Eq. (17) from the original RDE Eq. (9), after the elimination of Λ , $\hat{\phi}$ satisfies the following initial boundary value problem:⁽⁹⁾

$$\begin{cases} \frac{\partial \hat{\phi}}{\partial t} = K(1 + \tau \nabla^2 \hat{\phi}) & \text{in } D, \\ \frac{\partial \hat{\phi}}{\partial n} = 0 & \text{on } \partial D \setminus \partial \Gamma_N, \\ \hat{\phi} = 0 & \text{on } \partial \Gamma_N, \\ \hat{\phi}|_t = 0. \end{cases} \quad (18)$$

Owing to the Dirichlet boundary condition, analytical solution of $\hat{\phi}$ is not attainable. Notably, Eq. (18) does not depend on either the topological derivative or the value of ϕ . Consequently, solving

$\hat{\phi}$ just adds a one-time cost to the whole loop. In light of the time independence, we hereafter denote:

$$\hat{\phi} := \hat{\phi}|_{t+\Delta t}. \quad (19)$$

The volume constraint can then be viewed as an implicit equation for Λ :

$$g(\Lambda) = \int_D \chi_{\phi(\Lambda)} d\Omega - V_{\text{req}} = 0. \quad (20)$$

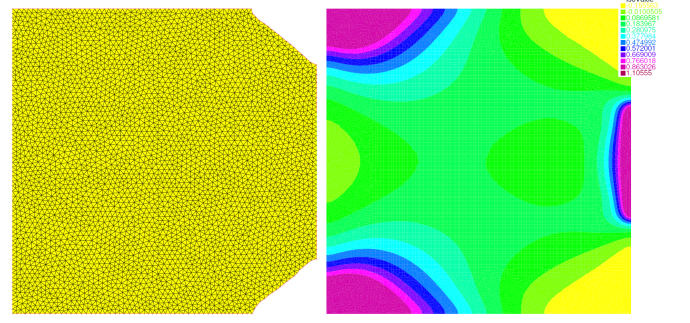
For Eq. (20), Newton-Raphson iteration is needed to find $\Lambda^{(9)}$. In the beginning of the optimization loop, as required to calculate the volume integration, a smoothed Heaviside function capable of converging to the rigorous Heaviside function has been adopted. Instead of an invariantly smoothed Heaviside function, a stepwise one is adopted:

$$H(\phi) = \max(\tanh(k\phi), 0). \quad (21)$$

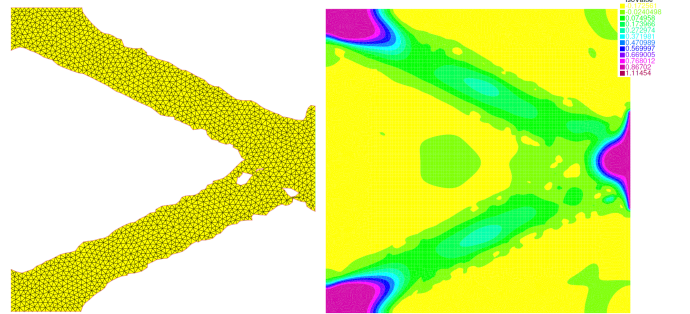
In the numerical implementation, we simply let $k = n^q + 1$ ($q = 0.5$) at the n th time step. Besides, all other conditions, such as the use of smoothed Heaviside function have been made identical in the comparison between the two volume constraint methods.

3. Results and discussions

In this section, results of topology optimization by using either the conventional or the recently proposed volume constraint method as introduced in the preceding section will be examined and discussed.

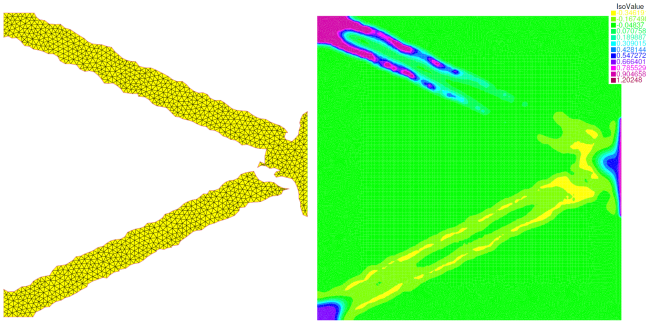


(a) Step 8



(b) Step 30

The volume constraint is set as $V_{\text{req}} = 0.05$, or 0.2 , or 0.5 , or 0.9



(c) Step 174

Fig. 2: The remeshed material domain (each left subfigure) and the corresponding ϕ distribution (each right subfigure) under the exact boundary representation by using the conventional augmented Lagrangian method (penalty parameter $r_1 = 0.1$). The volume constraint is $V_{\text{req}} = 0.2$. Convergence cannot be reached.

in this study. The other parameters can be found elsewhere⁽⁹⁾. The convergence criterion of structural topology optimization for ϕ is normally defined as

$$\|\phi|_{t+\Delta t} - \phi_t\|_{L^\infty} < 0.02. \quad (22)$$

Fig. 2 plots the remeshed material domain and the corresponding ϕ by applying the conventional volume constraint method. It has failed to reach convergence. During its optimization process, the remeshed and reconstructed domain has kept varying, and its volume is either much bigger or smaller than the required $V_{\text{req}} = 0.2$. At step 8 of Fig. 2, the reconstructed material domain is outlined by a smooth boundary. The corresponding ϕ contour also displays a quite smooth distribution. However, at step 30 in Fig. 2, zigzag patterns can be spotted all along its remeshed material boundary. The zigzag boundaries are also related to the mesh density. Under extremely fine meshes, both volume constraint methods result in almost no zigzag, while the conventional method still cannot attain convergence. Under rather coarse meshes, the recently proposed method can not only achieve convergence, but also suppress the zigzag pattern and hence enhance the smoothness. Likewise, the distribution of its level set function changes into a disordered state. The accumulated instability leads to the unnecessary insertion of holes in the place near the traction boundary. Finally, at step 174, the stress analysis is unable to proceed due to that the structure loses load-carrying capacity in the horizontal direction.

For the case of penalty parameter $r_1 = 0.1$ in the conventional way to constrain volume, the resulted volume ratio in Fig. 3 drops from 100% to near 20% and yet keeps fluctuating around the targeted ratio. Correlating with Fig. 2, it can be known that not only that the volume ratio is constantly varying, but the zigzag outline of the material domain is also evolving. As a consequence, the structural compliance in Fig. 3 has a considerable fluctuation before it

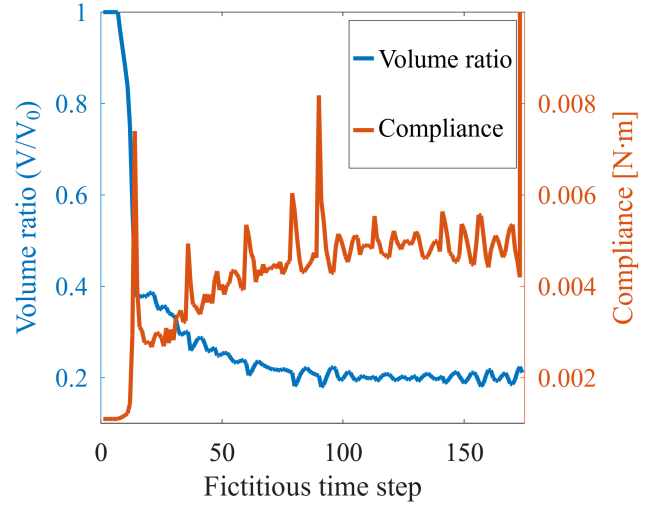
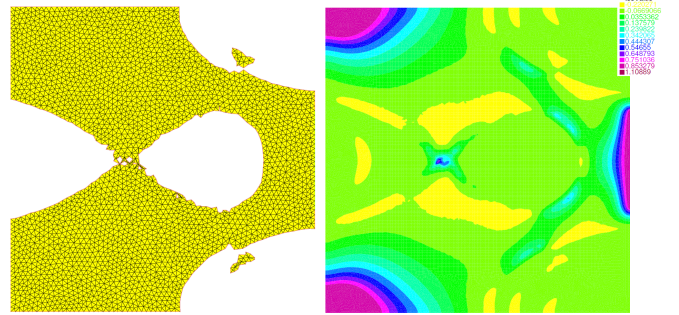
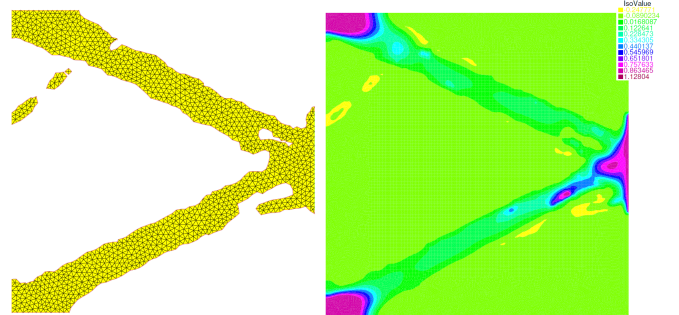


Fig. 3: The actual volume ratio of material and the structural compliance under the exact boundary representation by using the conventional augmented Lagrangian method (penalty parameter $r_1 = 0.1$). The second last structural compliance reaches 0.733 [N·m] before finally approaching infinity. The volume constraint is $V_{\text{req}} = 0.2$.

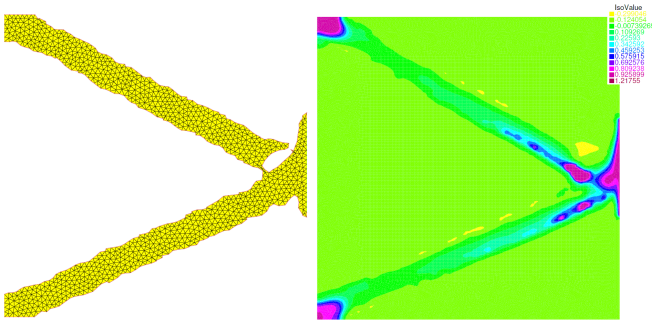
approaches infinity when the resulted structure totally loses load-carrying capacity.



(a) Step 8



(b) Step 30



(c) Step 70

Fig. 4: The remeshed material domain (each left subfigure) and the corresponding ϕ distribution (each right subfigure) under the exact boundary representation by using the conventional augmented Lagrangian method (penalty parameter $r_1 = 0.2$). The volume constraint is $V_{\text{req}} = 0.2$. Convergence cannot be reached either.

Once the penalty parameter in the conventional method of volume constraint is doubled in Fig. 4, the convergence still cannot be achieved. Comparing step 8 in Fig. 2 with that in Fig. 4, the larger penalty parameter has somehow accelerated the reduction of the material volume from the initial hole-free configuration. At the same time, the zigzag pattern along the material boundary occurs earlier than in Fig. 2. It is also faster for the optimization process to reach a failed structure, whose compliance approach infinity. Compared with Fig. 3, the volume ratio in Fig. 5 appears smoother and hence fewer spikes are seen in its structural compliance curve. It seems that the convergence issue is an inherent obstacle to achieving exact boundary representation by using conventional method of volume constraint.

Fig. 6 plots the remeshed material domain and the corresponding ϕ at different steps by using the recently proposed exact volume constraint method.⁽⁹⁾ Comparing step 8 in Fig. 6 with those in Fig. 2 and Fig. 4, the search process for the optimized structure is obviously more efficient by using the exact volume constraint method. In a sharp contrast, the boundary outline in Fig. 6 is almost free of zigzag patterns. Not only convergence has been achieved in Fig. 6, but also the final compliance of the structure is lower than that by using the SIMP method, whose boundary representation is based on density and therefore not exact. Since Newton-Raphson iteration is implemented, the volume and hence the overall optimization loop becomes much more stable.

At the beginning, the smoothed Heaviside function was involved in the volume integration from the distribution of ϕ . Therefore, the constraint is rather imposed on the volume ratio of the material that is defined by the smoothed Heaviside function. In our numerical implementation, the smoothed Heaviside function gradually approaches the real one during the optimization process. As a result, the actual volume ratio, as seen in Fig. 7, decreases from 100% to

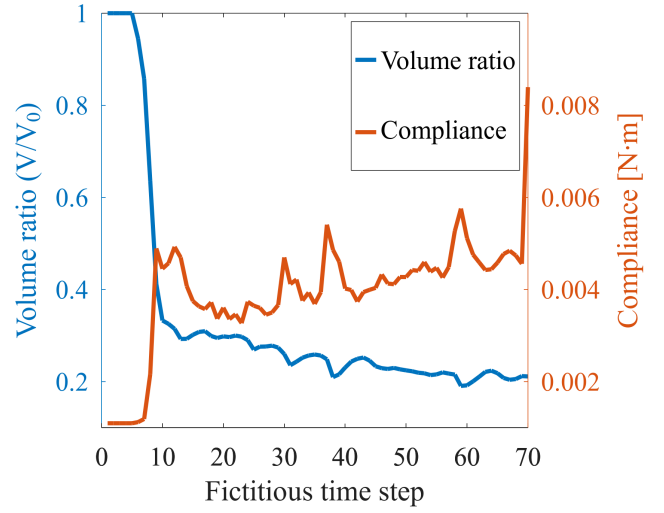


Fig. 5: The actual volume ratio of material and the structural compliance under the exact boundary representation by using the conventional augmented Lagrangian method (penalty parameter $r_1 = 0.2$). In the next optimization step, the final compliance would approach infinity. The volume constraint is $V_{\text{req}} = 0.2$.

20%. By applying the exact volume constraint method, the actual volume ratio swiftly turns into an almost horizontal line after just 20 steps. This is totally different from that in Fig. 3 or Fig. 5. The well-constrained volume leads to no spike and almost no fluctuation in the structural compliance curve. On the structural compliance curve, its initial rise is just due to the sudden reduction of the actual material volume.

Last but not least, the probable cause of the convergence issue is to be examined. From optimization step n to step $n + 1$, when $G_n \geq -q_n/r_n$ is assumed, the volume constraint equation at step $n + 1$ for the augmented Lagrangian method is:

$$\begin{cases} G_{n+1} = \int_D \chi(\phi_n(\Lambda_{n+1})) \, d\Omega - V_{\text{req}}. \\ \Lambda_{n+1} = \frac{1}{V} (q_n + r_n G_n) \end{cases} \quad (23)$$

It can be easily noted that since the update in Eq. (23) is akin to an explicit time-stepping scheme, instability would be built up inside the optimization loop. The change in the level set function ϕ_{n+1} with respect to ϕ_n is simply governed by:

$$\begin{aligned} \frac{\partial \phi_{n+1} - \partial \phi_n}{\partial t} \\ = K[-(\bar{\mathcal{T}}_{n+1} - \bar{\mathcal{T}}_n) + \Lambda_{n+1} - \Lambda_n + \tau \nabla^2 (\phi_{n+1} - \phi_n)] \end{aligned} \quad (24)$$

As shown in Fig. 8, interpolation error between the two meshes inevitably occurs during the remeshing of the actual material domain. In other words, this is caused by the term $\bar{\mathcal{T}}_{n+1} - \bar{\mathcal{T}}_n$ and cannot be fixed since Λ_{n+1} is explicitly determined from step $n+1$ in the conventional augmented Lagrangian method. In a sharp

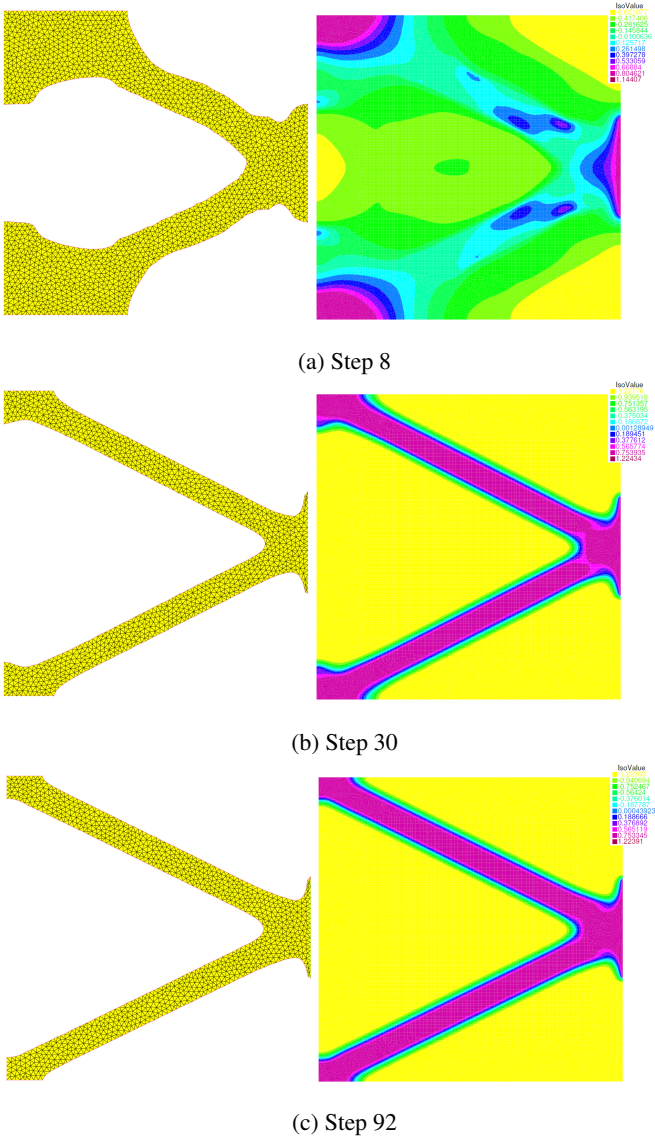


Fig. 6: The remeshed material domain (each left subfigure) and the corresponding ϕ distribution (each right subfigure) under the exact boundary representation by using the recently proposed exact volume constraint method. The volume constraint is $V_{\text{req}} = 0.2$. Convergence has been reached.

contrast, Λ_{n+1} in the recently proposed exact volume constraint method is determined by Newton-Raphson iteration at the current time step, and therefore it can offset the instability issue caused by $\bar{\mathcal{T}}_{n+1} - \bar{\mathcal{T}}_n$. Thanks to the implementation of Newton-Raphson iteration, the overall optimization process is stabilized and hence convergence can be attained.

Next, we replace the volume constraint from $V_{\text{req}} = 0.2$ with an extremely large one $V_{\text{req}} = 0.9$ or an extremely small one $V_{\text{req}} = 0.05$. For an extremely small constraint of volume, a deteriorated connectivity of the reconstructed domain Ω could occur horizontally due to the sudden decrease of the actual material volume. To solve this issue, one can either start from a rough estimation of the ϕ distribution such as the one from using a fixed and coarse mesh,

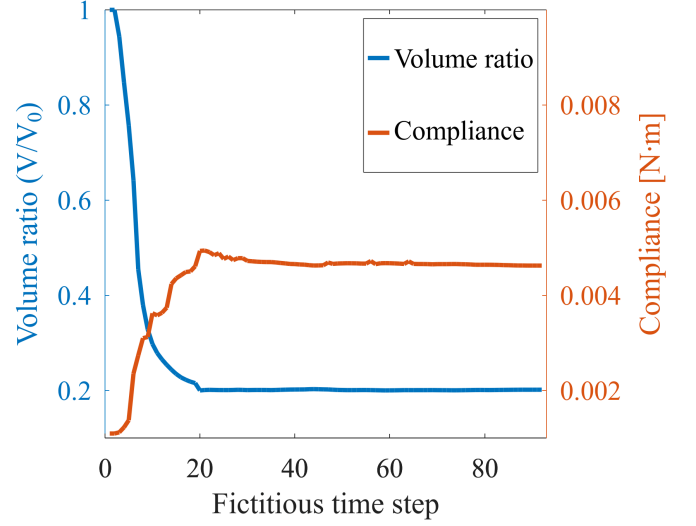


Fig. 7: The actual volume ratio of material and the structural compliance under the exact boundary representation by using the recently proposed exact volume constraint method.

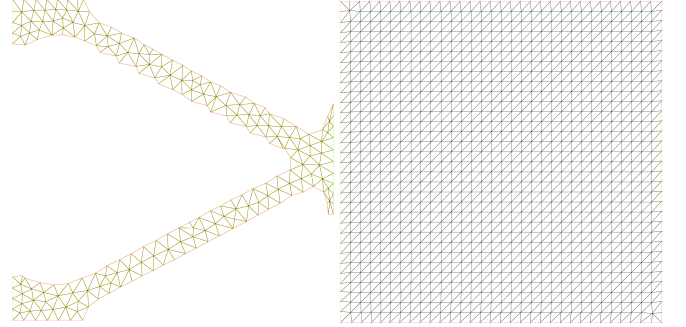


Fig. 8: The FEM mesh for the stress equilibrium (left subfigure) and that for the reaction-diffusion equation (RDE) of ϕ (right subfigure). Coarse meshes are shown here for better illustration.

or one can simply set the volume constraint at the n th step as:

$$V_{\text{req},n} = V_n + \beta(V_{\text{req}} - V_n). \quad (25)$$

Here $V_{\text{req},n}$ represents the volume constraint imposed at the n th optimization step, V_n is the actual material volume ratio at the n th step, V_{req} is the initial volume constraint, and $\beta \in [0, 1]$ is a coefficient to smooth the decrease of the actual volume. Initially $\beta = 0.5$, and at the final stage of optimization $\beta = 1.0$ ensures that $V_{\text{req},n} = V_{\text{req}}$, when V_n comes close enough to V_{req} (e.g. within 10%).

From now on, V_{req} is replaced by $V_{\text{req},n}$ in imposing the volume constraint at n th optimization step. Fig. 9 and Fig. 10 indicate that our approach of exact boundary representation (by using the exact volume constraint) is valid even for an extremely small volume constraint. The thin beam-like structure in Fig. 10 requires a fine mesh density (0.004) in remeshing, otherwise the mesh resolution would

not be enough for its slenderness.

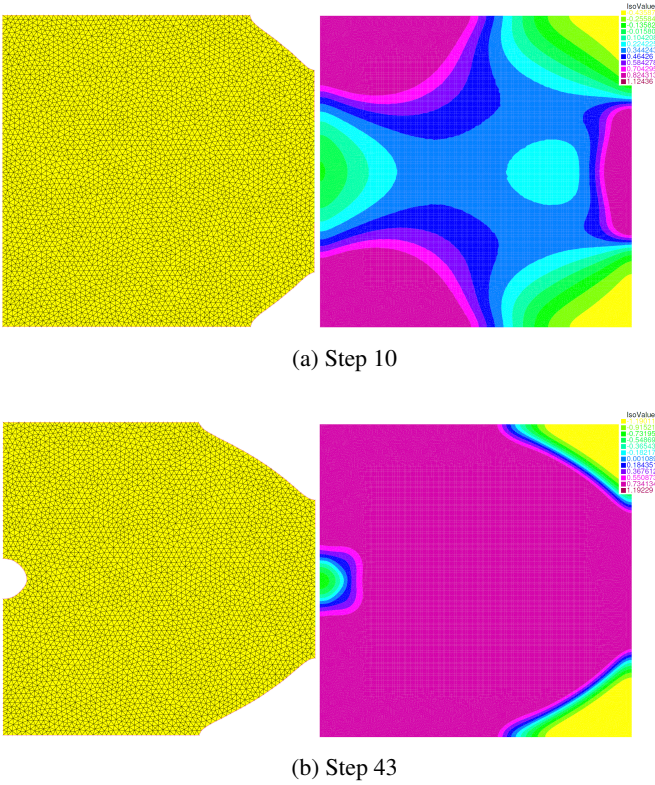


Fig. 9: The remeshed material domain (each left subfigure) and the corresponding ϕ distribution (each right subfigure) under the exact boundary representation by using the recently proposed exact volume constraint method. The volume constraint is $V_{\text{req}} = 0.9$. The compliance and actual volume ratio at Step 10 and Step 43 are 0.00110 [N·m] and 0.9601 and 0.00105 [N·m] and 0.8996, respectively.

Fig. 11 and Fig. 12 show that our approach of exact boundary representation (by using the exact volume constraint) is valid even when the aspect ratio in the horizontal direction becomes extremely large than the vertical direction. Under such a situation, the topology of the optimized structures are more complex since more holes are introduced. Overall, the structure near the boundary traction is seen slimmer than that near the fixed end. In Fig. 12, for the same reason, the same very fine mesh is adopted in remeshing, otherwise the mesh resolution would not be enough for the slenderness.

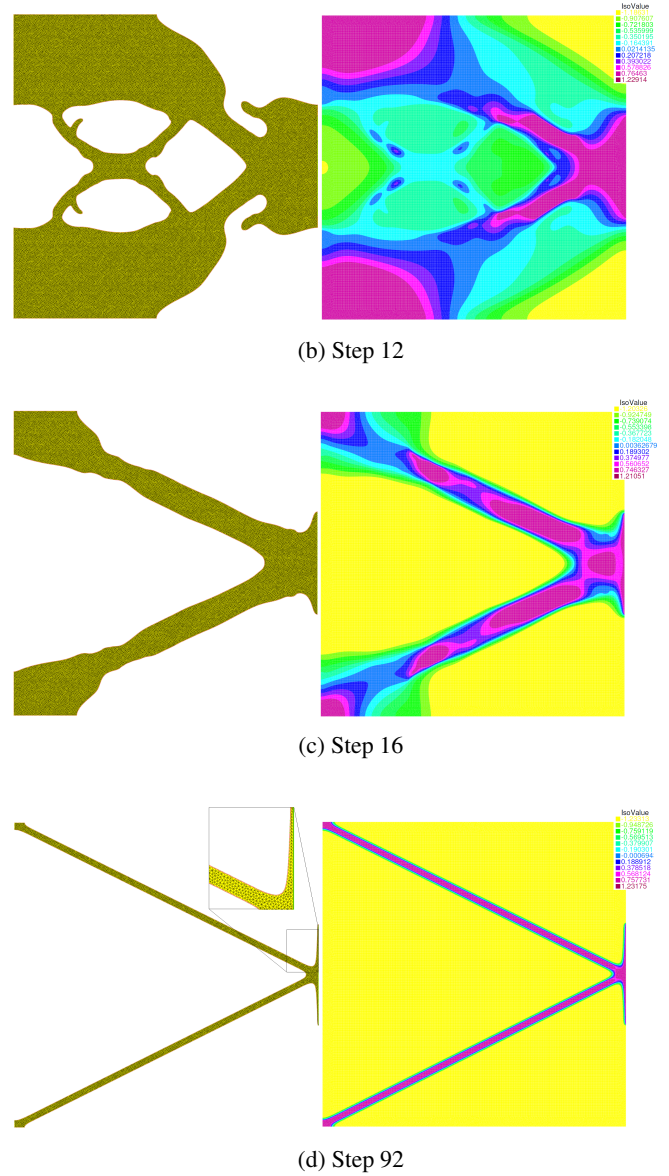
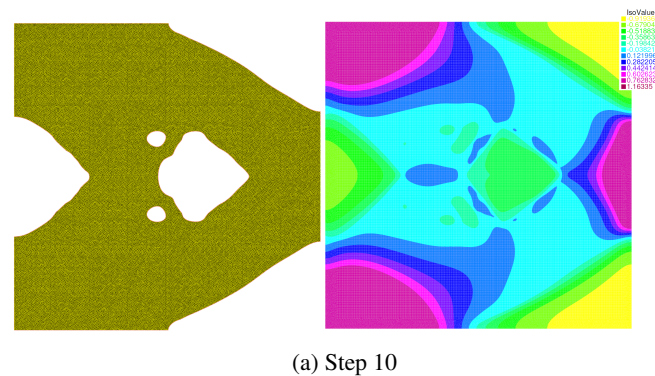
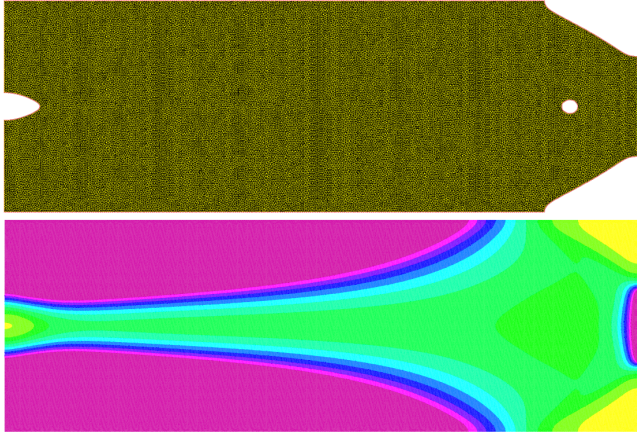


Fig. 10: The remeshed material domain (each left subfigure) and the corresponding ϕ distribution (each right subfigure) under the exact boundary representation by using the recently proposed exact volume constraint method. The volume constraint is $V_{\text{req}} = 0.05$. The compliance and actual volume ratio at Step 10, Step 12, Step 16, Step 30 and Step 92 are 0.001428 [N·m] and 0.7333, 0.004964 [N·m] and 0.5533, 0.004917 [N·m] and 0.2400, and 0.02125 [N·m] and 0.04995, respectively. The zoom-in inset shows the adopted fine mesh.

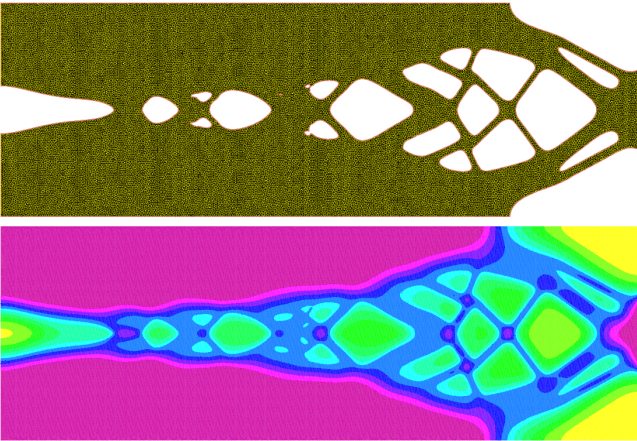
4. Conclusions

Regarding the topology optimization with exact boundary representation, we have further investigated those aforementioned issues in Section 1 such as the influence of penalty parameters in the conventional volume constraint method, the extreme setup of constrained volume and the aspect ratio of the design domain. It is indicated that the difference between the FEM mesh for the stress equilibrium and that for the reaction-diffusion equation (RDE) of level

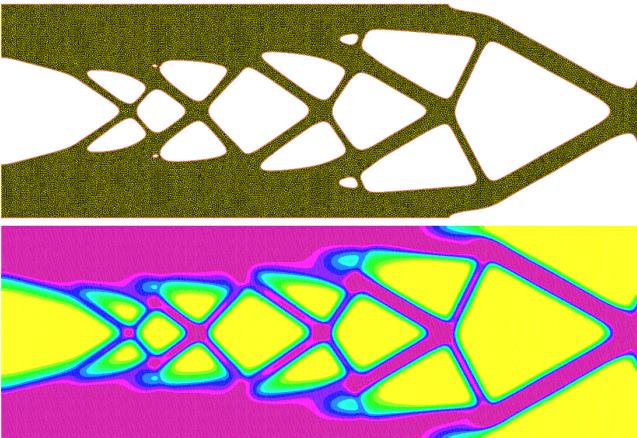
set function could be responsible for the convergence issue. Since the conventional volume constraint method is akin to an explicit time-stepping scheme, instability is built up inside the optimization loop. In this regard, the new exact volume constraint method can stabilize the overall optimization and hence attain the convergence.



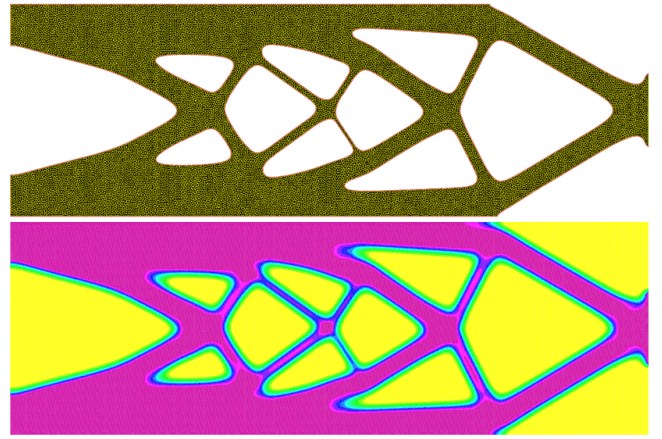
(a) Step 20



(b) Step 40

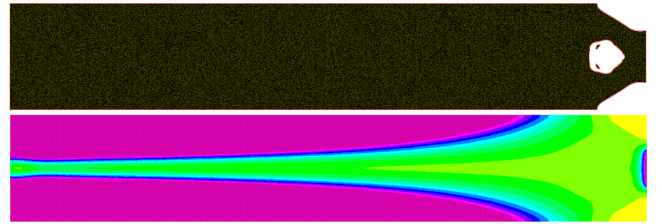


(c) Step 60

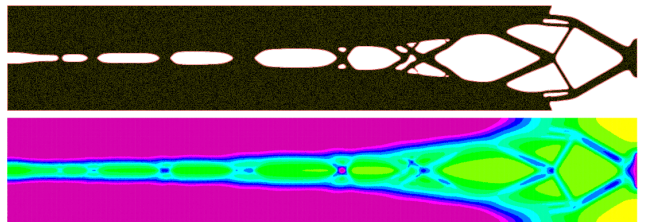


(d) Step 167

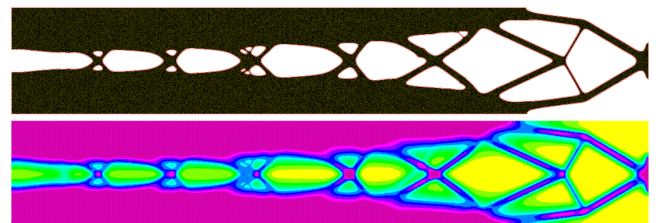
Fig. 11: The remeshed material domain (each upper subfigure) and the corresponding ϕ distribution (each lower subfigure) under the exact boundary representation by using the recently proposed exact volume constraint method. The volume constraint is $V_{\text{req}} = 0.5$, and the aspect ratio of design domain is 3:1. The compliance and actual volume ratio at Step 20, Step 40, Step 60 and Step 167 are 0.01871 [N·m] and 0.7709, 0.02017 [N·m] and 0.6534, 0.02570 [N·m] and 0.5004, and 0.02518 [N·m] and 0.04997, respectively.



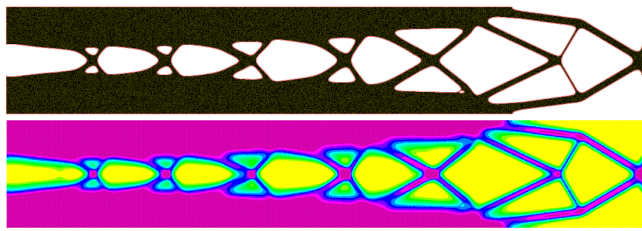
(a) Step 30



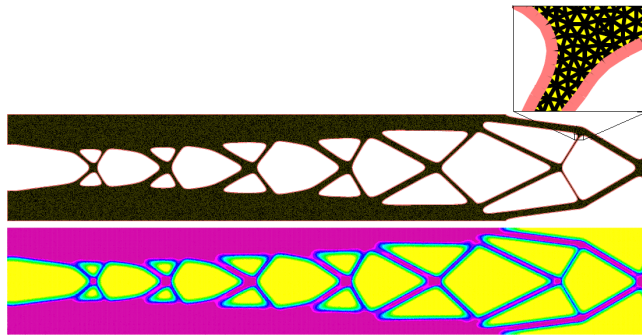
(b) Step 40



(c) Step 50



(d) Step 60



(e) Step 86

Fig. 12: The remeshed material domain (each upper subfigure) and the corresponding ϕ distribution (each lower subfigure) under the exact boundary representation by using the recently proposed exact volume constraint method. The volume constraint is $V_{\text{req}} = 0.5$, and the aspect ratio of design domain is 6:1. The compliance and actual volume ratio at Step 30, Step 40, Step 50, Step 60 and Step 86 are 0.1351 [N·m] and 0.7333, 0.1483 [N·m] and 0.7467, 0.1547 [N·m] and 0.6416, 0.1637 [N·m] and 0.5934 and 0.1747 [N·m] and 0.5005, respectively. The zoom-in inset shows the adopted fine mesh.

5. Acknowledgements

The author Y. Cui acknowledges the support of the Makimakoto Commemorative Research Grant and Nagoya University Faculty of Engineering Support Research Grant.

Reference

- (1) Bendsøe, M.P., Sigmund, O.. Material interpolation schemes in topology optimization. *Archive of Applied Mechanics (Ingenieur Archiv)* Vol.69, No.(9-10), (1999), pp.635-654. doi:10.1007/s004190050248.
- (2) Bendsøe, M.P., Sigmund, O.. *Topology Optimization*. Berlin, Heidelberg: Springer Berlin Heidelberg, (2004), doi:10.1007/978-3-662-05086-6.
- (3) Yamada, T., Izui, K., Nishiwaki, S., Takezawa, A.. A topology optimization method based on the level set method incorporating a fictitious interface energy. *Computer Methods in Applied Mechanics and Engineering* Vol.199, No.45-48, (2010), pp.2876-2891. doi:10.1016/j.cma.2010.05.013.
- (4) Emmendoerfer, H., Silva, E.C.N., Fancello, E.A.. Stress-constrained level set topology optimization for design-dependent pressure load problems. *Computer Methods in Applied Mechanics and Engineering* Vol.344, (2019), pp.569-601. doi:10.1016/j.cma.2018.10.004.
- (5) Zhang, Z., Xie, Y.M., Li, Q., Zhou, S.. A reaction-diffusion based level set method for image segmentation in three dimensions. *Engineering Applications of Artificial Intelligence* Vol.96, (2020), pp.103998. doi:10.1016/j.engappai.2020.103998.
- (6) Li, H., Yamada, T., Jolivet, P., Furuta, K., Kondoh, T., Izui, K., Nishiwaki, S.. Full-scale 3D structural topology optimization using adaptive mesh refinement based on the level-set method. *Finite Elements in Analysis and Design* Vol.194, (2021), pp.103561. doi:10.1016/j.finel.2021.103561.
- (7) Zhuang, Z., Xie, Y., Zhou, S., A reaction diffusion-based level set method using body-fitted mesh for structural topology optimization. *Computer Methods in Applied Mechanics and Engineering* Vol.381, No.1 (2021), pp. 113829. doi: https://doi.org/10.1016/j.cma.2021.113829.
- (8) Zhuang, Z., Xie, Li, Q., Y., Zhou, S., Body-fitted bi-directional evolutionary structural optimization using nonlinear diffusion regularization. *Computer Methods in Applied Mechanics and Engineering* Vol.396, No.1 (2022), pp. 115114. https://doi.org/10.1016/j.cma.2022.115114.
- (9) Cui, Y., and Takahashi, T., and Matsumoto, T., An exact volume constraint method for topology optimization via reaction-diffusion equation (May 17, 2022). Available at SSRN: https://ssrn.com/abstract=4112073 or http://dx.doi.org/10.2139/ssrn.4112073.
- (10) Lopes, C.G., Santos, R.B.d., Novotny, A.A.. Topological derivative based topology optimization of structures subject to multiple loadcases. *Latin American Journal of Solids and Structures* Vol.12, No.5, (2015), pp.834-860. doi:10.1590/1679-78251252.
- (11) Hestenes, M. R.. Multiplier and gradient methods. *Journal of Optimization Theory and Applications*, Vol. 4, No.5, (1969), pp.303-320. doi:10.1007/BF00927673.
- (12) Rockafellar, R. T.. The multiplier method of Hestenes and Powell applied to convex programming. *Journal of Optimization Theory and Applications*, Vol.12, No.6, (1973), pp.555-562. doi:10.1007/BF00934777.
- (13) Powell M. J. D.. Algorithms for nonlinear constraints that use Lagrangian functions. *Mathematical Programming*, Vol. 14, (1978), pp.224-248. doi:10.1007/BF01588967.
- (14) Hecht, F.. New development in freefem++. *Journal of Numerical Mathematics* Vol.20, No.3-4, (2012), pp. 251-265, doi:10.1515/jnum-2012-0013.

- (15) Jolivet, P., Dolean, V., Hecht, F., Nataf, F., Pru' Homme, C., Spillane, N.. High performance domain decomposition methods on massively parallel architectures with freefem++. *Journal of Numerical Mathematics* vol. 20, no. 3-4, (2012), pp. 287-302. doi:10.1515/jnum-2012-0015.
- (16) Kim, C., Jung, M., Yamada, T., Nishiwaki, S., Yoo, J.. FreeFEM++ code for reaction-diffusion equation-based topology optimization: for high-resolution boundary representation using adaptive mesh refinement. *Structural and Multidisciplinary Optimization* Vol. 62, No.1, (2020), pp.439-455. doi:10.1007/s00158-020-02498-3